Check for updates

View Article Online
View Journal

Nanoscale

Accepted Manuscript

This article can be cited before page numbers have been issued, to do this please use: H. Han, H. Yang and S. Liu, *Nanoscale*, 2025, DOI: 10.1039/D5NR02857D.

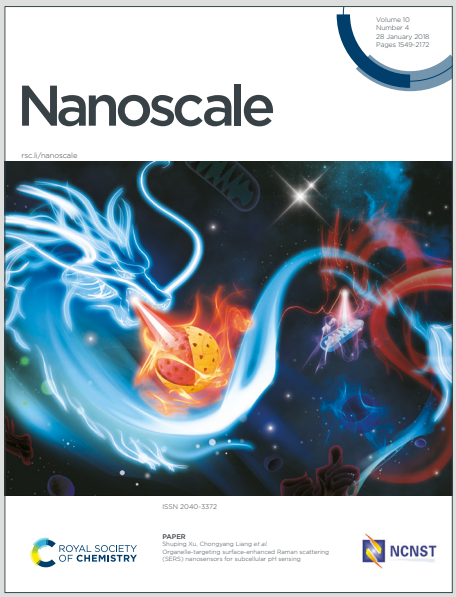

This is an Accepted Manuscript, which has been through the Royal Society of Chemistry peer review process and has been accepted for publication.

Accepted Manuscripts are published online shortly after acceptance, before technical editing, formatting and proof reading. Using this free service, authors can make their results available to the community, in citable form, before we publish the edited article. We will replace this Accepted Manuscript with the edited and formatted Advance Article as soon as it is available.

You can find more information about Accepted Manuscripts in the Information for Authors.

Please note that technical editing may introduce minor changes to the text and/or graphics, which may alter content. The journal's standard Terms & Conditions and the Ethical guidelines still apply. In no event shall the Royal Society of Chemistry be held responsible for any errors or omissions in this Accepted Manuscript or any consequences arising from the use of any information it contains.

ROYAL SOCIETY OF CHEMISTRY

rsc.li/nanoscale

View Article Online
DOI: 10.1039/D5NR02857D

Tailoring Electron Redistribution and Hydrogen Adsorption in Epitaxial MnTe/Cr_2Te_3 Semiconductor/Metal Heterojunction for Highly Efficient Hydrogen Evolution Catalysis

Hao Han[a], Huan Yang[b*], Shichuang Liu[c]

[a] *School of Mechatronic Engineering, Xi'an Technological University, Xi'an 710021, China*

[b] *School of Materials Science and Engineering, Shanxi Normal University, Taiyuan 030032, China.*

[c] *College of Mechanical and Transport Engineering, Taiyuan University of Technology, Taiyuan 030024, China*

*E-mail: yanghuan611711@163.com (H. Yang).

Published on 16 August 2025. Downloaded by Yunnan University on 8/23/2025 4:22:07 PM.

Nanoscale Accepted Manuscript

ABSTRACT

Electronic structure engineering and interface chemistry is critical for optimizing hydrogen evolution reaction (HER) electrocatalysts. Here, we report a solution-based synthesis of Cr-doped MnTe nanowires and a Cr_2Te_3/MnTe/Cr_2Te_3 metal/semiconductor/metal heterojunctions that achieves outstanding HER performances. The epitaxial interface, defined by coherent lattice alignment between MnTe and Cr_2Te_3, enables directional electron transfer from the metallic metallic Cr_2Te_3 caps to the MnTe semiconductor, as supported by XPS and Bader charge analyses. DFT calculations reveal that Cr doping enhances conductivity and introduces active electronic states, while the heterojunction simultaneously optimizes hydrogen adsorption free energy (ΔG_{H*}) and reduces HER reaction barriers. As a result, the catalyst achieves a low overpotential of -0.354 V at 10 mA cm^{-2} and a small Tafel slope of 53.9 mV dec^{-1}, surpassing its individual components. This work offers strategic guidance for designing highly efficient non-noble metal HER electrocatalysts via interface engineering and electronic structure tuning.

Keywords: Liquid-phase synthesis; Cr-doped MnTe nanorods; MnTe/Cr_2Te_3 semiconductor/metal

View Article Online
DOI: 10.1039/D5NR02857D

heterostructures; HER

1. Introduction

Hydrogen (H_2), as a clean, efficient, and sustainable energy carrier, holds great promise as a future alternative to fossil fuels.[1] Among the various hydrogen production technologies, electrochemical water splitting—particularly the hydrogen evolution reaction (HER)—has attracted considerable attention due to its high efficiency, environmental friendliness, and scalability.[2] Platinum (Pt)-based catalysts are widely regarded as the most effective HER electrocatalysts owing to their ultra-low overpotential and high current densities.[3] However, the high cost and limited abundance of Pt severely limit its large-scale application.[4] Therefore, the development of highly active, cost-effective, and earth-abundant non-noble metal HER catalysts remains a critical challenge in this field.

Transition metal chalcogenides (TMCs), including sulfides, selenides, and tellurides, have emerged as promising HER electrocatalysts due to their tunable electronic structures, abundant active sites, and excellent charge transport properties.[5-7] Among them, transition metal tellurides (e.g., MnTe) exhibit superior electrocatalytic performance compared to their sulfide and selenide counterparts. This can be attributed to their unique *d*-electron configurations, strong covalent metal-tellurium bonding, and inherently electrical conductivity.[8-10] Moreover, the large atomic radius and low electronegativity of Te promote electronic delocalization and significantly facilitate efficient charge transport.[11] Recent studies have also uncovered spin-related phenomena in MnTe, such as altermagnetism, offering new opportunities for catalytic modulation.[8] Despite these advantages, pristine MnTe suffers from sluggish HER kinetics due to suboptimal hydrogen adsorption free energy and limited exposure of catalytic sites .[12] Various strategies—such as defect engineering,

Published on 16 August 2025. Downloaded by Yunnan University on 8/23/2025 4:22:07 PM.

Nanoscale Accepted Manuscript

View Article Online
DOI: 10.1039/D5NR02857D

Published on 16 August 2025. Downloaded by Yunnan University on 8/23/2025 4:22:07 PM.

Nanoscale Accepted Manuscript

conductivity enhancement, heterointerface construction, and electronic structure modulation—have been explored to address these issues.[13-21] For example, Yang *et al.* developed RhP_2/Rh heterostructures embedded in N,P co-doped graphene, where interfacial electron transfer from metallic Rh to semiconductive RhP_2 effectively optimized the hydrogen binding energy on Rh sites.[21] However, achieving precise regulation of the electronic configuration of MnTe while simultaneously optimizing both charge transport and hydrogen adsorption remains a critical challenge.

To address these issues, we propose a solution-based strategy to tune the electronic structure of MnTe via Cr doping. By precisely controlling the $Cr(acac)_3$ concentration ($0 \leqslant x \leqslant 10$ at.%), we successfully synthesize 5% Cr-doped MnTe nanowires, and further constructed a one-dimensional Cr_2Te_3/MnTe/Cr_2Te_3 metal/semiconductor/metal heterojunction via in situ epitaxial growth (10%). Electrochemical measurements reveal that 5% Cr doping and MnTe/Cr_2Te_3 heterojunction formation all can improve catalytic activity, with the heterostructure exhibiting the highest HER performance. Density functional theory (DFT) calculations further indicate that the heterojunction improves electronic conductivity and charge transport, promotes interfacial charge transfer, optimizes the ΔG_{H^*}, and reduces key energy barriers along the HER pathway, thereby delivering outstanding electrocatalytic performance.

2. Experimental

Materials

Manganese (II) acetylacetonate [$Mn(acac)_2$, 95%], tellurium powder (Te, 99.5%), chromium (III) acetylacetonate [$Cr(acac)_3$, 98%], and trioctylphosphine (TOP, 90%) were supplied by Alfa Aesar. Oleylamine (OLA, 96%) was obtained from Energy Chemical. Hexane (99.5%) and ethanol

View Article Online
DOI: 10.1039/D5NR02857D

(99.7%) was purchased from Tianjin Kermel and Guangfu. All chemicals and solvents were used as received without any further purification.

Synthesis

A certain amount of $Cr(acac)_3$ powder [with nominal Cr atomic percentage x = Cr/(Cr + Mn) × 100%, where x = 0, 5, or 10 at.%], $Mn(acac)_2$ powder and 20 mL OLA were added to a 100 mL four-necked flask, in which the total amount of precursor $Cr(acac)_3$ and $Mn(acac)_2$ was 2.8 mmol. Here, "x" denotes the nominal Cr content based on precursor feeding ratio, not the actual Cr concentration in the final product. After stirring for 30 minutes under a nitrogen atmosphere, the mixture was heated to 120 °C and held for 20 minutes to remove low-boiling components. A 5 mL TOP solution containing 3.6 mmol of Te powder was then rapidly injected. The reaction mixture was heated to reflux (320 °C) at a rate of 5 °C/min and maintained for 2 hours. After cooling to room temperature, excess ethanol was added to precipitate the product, which was collected by centrifugation at 8000 rpm for 5 min and washed three times with hexane and ethanol. The final product was dispersed in hexane for further characterization.

Characterizations and electrochemical measurements

The phase structures were identified by using powder X-ray diffraction (XRD, D8 Advance) with a Cu Kα radiation source (λ = 0.154 nm). The morphologies and element contents were investigated by scanning electron microscope (SEM, JSM-7500F), transmission electron microscope (TEM, JEM-F2100) equipped with energy-dispersive X-ray spectroscope (EDX). High-resolution TEM (HRTEM) images, elemental mappings and selected area electron diffraction (SAED) patterns were collected using STEM equipped with spherical aberration correctors (JEM ARM200F). The chemical states of the obtained catalysts were recorded by X-ray photoelectron spectroscopy (XPS,

Published on 16 August 2025. Downloaded by Yunnan University on 8/23/2025 4:22:07 PM.

Nanoscale Accepted Manuscript

View Article Online
DOI: 10.1039/D5NR02857D

Thermo Scientific K-Alpha), with the C1s peak (284.6 eV) being used as a reference standard.

All the electrochemical measurements were carried out on a CHI 660E electrochemical workstation (CH Instruments, Inc.) with a standard three-electrode setup, the electrolyte used was 0.5 M H_2SO_4. A glassy carbon electrode (GCE, 4 mm diameter) coated with catalyst ink served as the working electrode, a standard Ag/AgCl electrode was used as the reference electrode, and a Pt wire was employed as the counter electrode. All potentials in this work were converted to the reversible hydrogen electrode (RHE) scale.

Computational method:

All DFT calculations were carried out using the VASP package[22,23] with the GGA-PBE functional[24] and the PAW method [25]. A plane-wave energy cutoff of 450 eV was applied. The MnTe (110) and Cr_2Te_3 (300) surfaces were used to construct the MnTe/Cr_2Te_3 heterojunction model. A vacuum layer of 20 Å was introduced along the z-axis to avoid spurious interlayer interactions. Geometry optimizations were performed with an energy convergence threshold of 10^{-5} eV and a force tolerance of 0.03 eV/Å. The Brillouin zone was sampled using a $5 \times 5 \times 1$ Monkhorst-Pack k-point mesh.

Hydrogen adsorption free energy (ΔG_{H^*}) was calculated to evaluate HER activity on MnTe and MnTe/Cr_2Te_3 heterostructure surfaces. Electronic properties were analyzed via total and partial DOS, Bader charge analysis, and charge density difference maps calculations to elucidate the effects of Cr doping and interfacial coupling on charge redistribution and HER reaction mechanisms.

3. Results and discussions

3.1. Catalyst Synthesis and Structural Characterization

To modulate the electronic structure and interface effects of MnTe, a series of Cr-doped MnTe chalcogenide catalysts were synthesized via a liquid-phase method by adjusting the molar ratio of

Published on 16 August 2025. Downloaded by Yunnan University on 8/23/2025 4:22:07 PM.

Nanoscale Accepted Manuscript

View Article Online
DOI: 10.1039/D5NR02857D

$Cr(acac)_3$ precursor (x = 0-10 at.%). The XRD patterns of the samples in the 2θ range of 20°-60° are shown in Fig. 1a. For x = 0, all diffraction peaks match well with hexagonal MnTe (JCPDS: 18-0814), without impurity peaks from Mn or Te oxides, indicating high phase purity. TEM images (Figs. 1c,d and S1) show that the sample consists of uniform nanowires with diameters around 80 nm and lengths up to 10 μm. High-resolution TEM (Fig. 1e) reveals the lattice spacing is 0.336 nm, corresponding to the (002) plane of hexagonal MnTe. This result is consistent with the SAED pattern shown in Fig. 1f, confirming the high crystallinity of the pure MnTe sample.

As the Cr doping content increases, the product still maintains a nanowire morphology (Figs. 1g,h, sample x = 5%). The nanowires exhibit diameters of approximately 100 nm and lengths ranging from 8 to 10 μm. HRTEM analysis (Fig. 1i) reveals that the (002) interplanar spacing decreases to 0.320 nm, slightly smaller than that of the undoped MnTe (0.336 nm). This reduction can be attributed to the substitution of Mn^{2+} ionic (66 pm) by the smaller Cr^{3+} ionic (62 pm) in the MnTe lattice. Additionally, elemental mapping (Fig. 1j) confirms the uniform distribution of Mn, Cr, and Te within individual nanowires. Moreover, as shown in the enlarged XRD patterns (Fig. 1b), the (101) peak of MnTe shifts from 28.2° to 28.4° at x = 5%, indicating a shift toward higher diffraction angles, which is consistent with the HRTEM observations (Fig. 1i). This confirms that Cr^{3+} cations successfully substitute Mn^{2+} cations in the MnTe lattice.

Published on 16 August 2025. Downloaded by Yunnan University on 8/23/2025 4:22:07 PM.

Nanoscale Accepted Manuscript

View Article Online
DOI: 10.1039/D5NR02857D

Published on 16 August 2025. Downloaded by Yunnan University on 8/23/2025 4:22:07 PM.

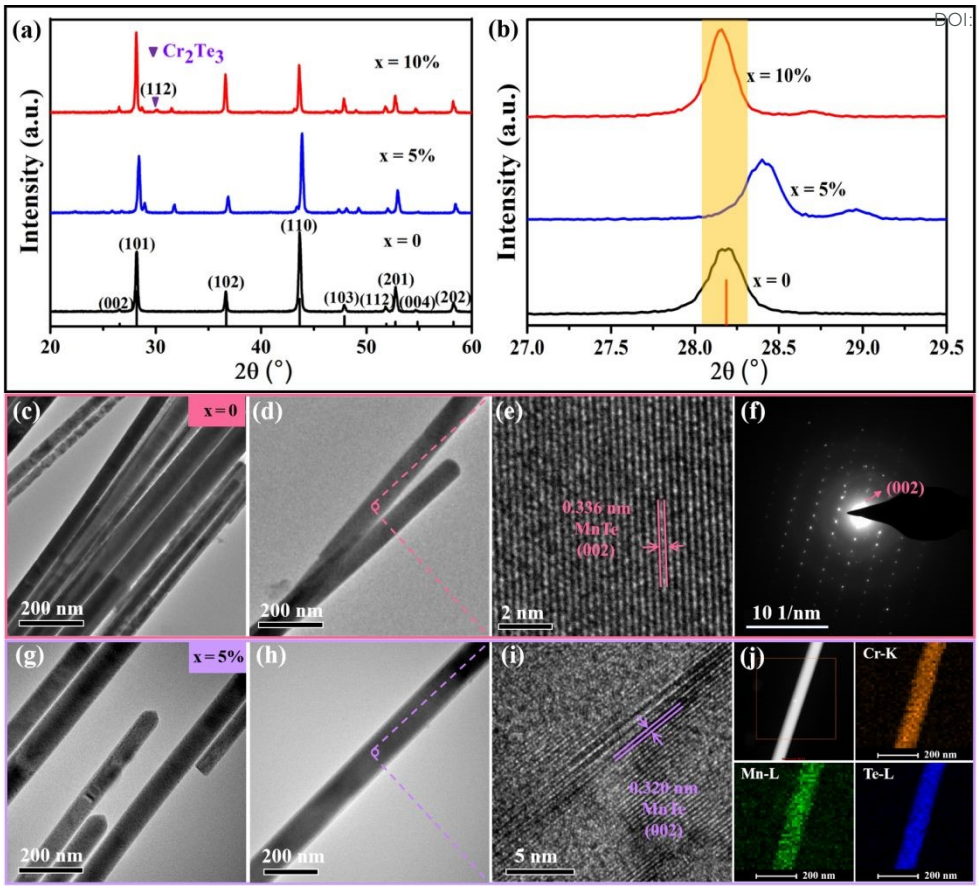

Fig. 1. (a) The XRD patterns of different $MnTe_{1-x}Cr_xTe$ samples (x = 0%, 5%, 10%). (b) Enlarged XRD view of MnTe (101) diffraction peak. (c,d) TEM images, (e) HRTEM image, and (f) SAED pattern of pristine MnTe nanowires. (g,h) TEM images, (i) HRTEM image, and (j) elemental mapping of Cr-doped MnTe nanowires (x = 5%).

When the Cr content increases to x = 10%, the XRD pattern retains the characteristic peaks of hexagonal MnTe (JCPDS: 86-1022), but a minor peak appears at $2\theta \approx 30°$, corresponding to the (112) plane of Cr_2Te_3 (JCPDS: 29-0458), as shown in Fig. 1a. This observation suggests the coexistence of MnTe and Cr_2Te_3 crystalline phases in the x = 10% sample. The corresponding product (Figs. 2a-c) exhibits a nanorod morphology with an average diameter of ~100 nm and length of ~500 nm, featuring distinct caps at both ends. Elemental mapping (Fig. 2d) shows that Cr is enriched at the nanorod ends, Mn is confined to the rod body, and Te is uniformly distributed throughout the entire

Nanoscale Accepted Manuscript

View Article Online
DOI: 10.1039/D5NR02857D

heterojunction. These results indicate that the one-dimensional heterojunction consists of a MnTe nanorod core with Cr_2Te_3 nanocaps at both ends. High-resolution TEM images (Figs. 2g,h) reveal a coherent and well-defined epitaxial interface between MnTe and Cr_2Te_3. The lattice spacings in the cap region are measured to be 0.307 nm and 0.196 nm, corresponding to the (004) and (300) planes of hexagonal Cr_2Te_3, while the body region shows the spacings of 0.336 nm and 0.206 nm, attributed to the (002) and (110) planes of hexagonal MnTe. At the interface, the lattice fringes are continuous and free of distortion or defects. Moreover, the alignment of specific lattice planes—MnTe (110) and Cr_2Te_3 (300)—along a common [001] growth direction provides direct evidence of epitaxial relationship. Furthermore, we quantified the lattice mismatch between MnTe (110) and Cr_2Te_3 (300) planes based on HRTEM data, yielding a small mismatch of ~4.85%. Additionally, DFT calculations show a negative interface formation energy of -0.62 J/m^2 (Fig. S3), indicating a thermodynamically favorable and coherent MnTe/Cr_2Te_3 interface.

Cross-sectional line scan analysis in region i (Fig. 2i) provides further evidence for phase separation.[26] The Mn and Te signals vary synchronously with an approximate atomic ratio of 1:1, whereas Cr is completely absent from the rod body. This confirms that Cr^{3+} does not incorporate into the MnTe lattice, but instead remains localized in the Cr_2Te_3 caps. In the single heterojunction nanorod (Fig. 2c), the total atomic percentages of Cr, Mn, and Te are 9.78%, 41.03%, and 49.19%, respectively, which closely match the theoretical composition (10%:40%:50%), as shown in Fig. 2j.

Published on 16 August 2025. Downloaded by Yunnan University on 8/23/2025 4:22:07 PM.

Nanoscale Accepted Manuscript

View Article Online
DOI: 10.1039/D5NR02857D

Published on 16 August 2025. Downloaded by Yunnan University on 8/23/2025 4:22:07 PM.

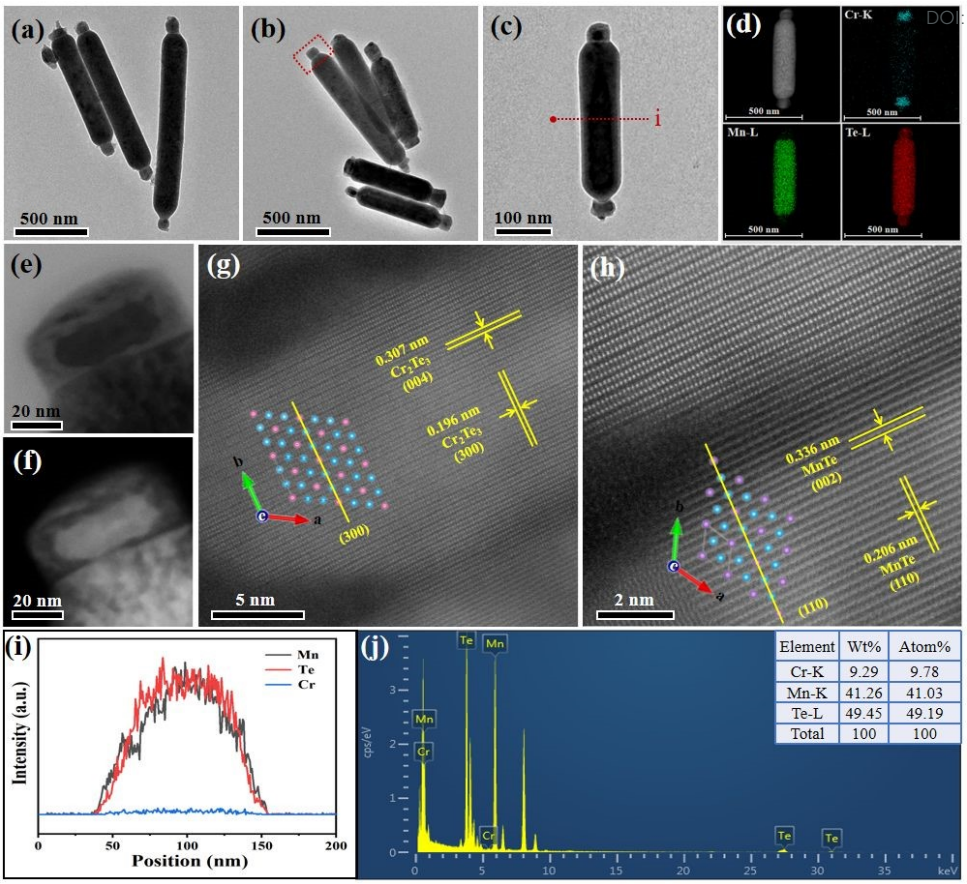

Fig. 2. (a-c) TEM images, (d) Elemental mapping, (e,f) Enlarged TEM images, (g,h) HRTEM images of Cr_2Te_3/MnTe/Cr_2Te_3 heterojunction (x = 10%). (i) Cross-sectional line scan EDX from i region in Fig. (c). (j) EDX of single nanorod heterojunction in Fig. (c).

To further confirm the formation of the Cr_2Te_3/MnTe/Cr_2Te_3 heterojunction and investigate the interfacial electronic interactions, X-ray photoelectron spectroscopy was conducted on the x = 10% sample. High-resolution spectra of Cr-2*p*, Mn-2*p*, and Te-3*d* are shown in Figs. 3a-c. For the Cr_2Te_3/MnTe/Cr_2Te_3 heterojunction, the peaks at approximately 576.5 and 586.8 eV correspond to Cr^{3+} $2p_{3/2}$ and $2p_{1/2}$ (Figs. 3a), while those at ~640.8 and 652.7 eV correspond to Mn^{2+} $2p_{3/2}$ and $2p_{1/2}$ (Figs. 3b). Compared to Cr^{3+} binding energies in pure Cr_2Te_3 (576.2 and 586.5 eV),[27] the Cr^{3+} peaks in the heterostructure exhibit a positive shift of ~0.3 eV. Meanwhile, the Mn^{2+} binding energies in the heterostructure (Fig. 3b) are ~0.2 eV lower than those of Mn^{2+} in pure MnTe (641.0 and 652.9

Nanoscale Accepted Manuscript

View Article Online
DOI: 10.1039/D5NR02857D

eV),[28] This suggests electron transfer from Cr^{3+} to MnTe across the Cr_2Te_3/MnTe heterointerface, resulting in electron-enriched MnTe. The Te-*3d* peaks (Fig. 3c) in heterojunction appears at 572.3 and 582.6 eV (Te^{2-} $3d_{5/2}$ and $3d_{3/2}$), and lie between those of pure Cr_2Te_3 (572.5 and 582.8 eV) and MnTe (572.0 and 582.3 eV), further corroborating charge redistribution of Te anions at the interface.

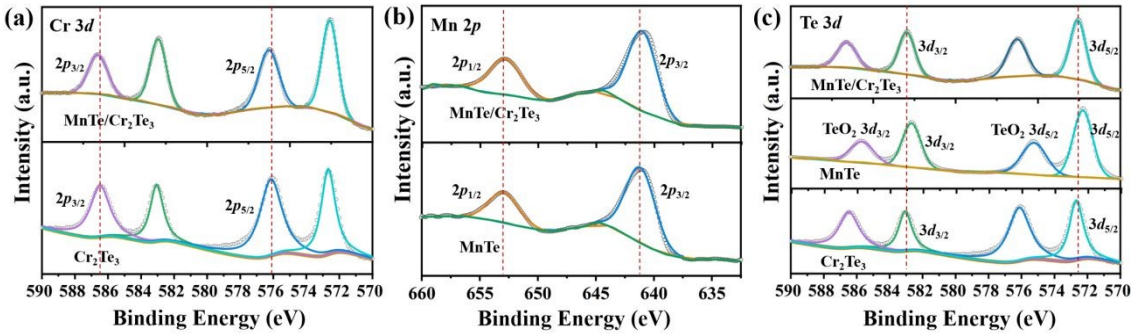

Fig. 3. (a-c) High-resolution XPS spectra for Mn 2*p*, Cr 2*p*, and Te 3*d*.

3.2. HER Performance

To systematically investigate the impact of Cr doping and heterostructure construction on HER performance, linear sweep voltammetry (LSV), Tafel analysis, electrochemical impedance spectroscopy (EIS), and chronopotentiometric stability measurements were performed. All electrochemical tests were conducted in 0.5 M H_2SO_4 using a glassy carbon electrode modified with the synthesized nanomaterials at a scan rate of 5 mV s^{-1}. As shown in Fig. 4a, the Cr_2Te_3/MnTe/Cr_2Te_3 heterojunction exhibited the highest HER activity, requiring an overpotential of -0.354 V to achieve a current density of 10 mA cm^{-2}, with a Tafel slope as low as 53.9 mV dec^{-1}. This performance was significantly better than that of pure MnTe (-0.547 V, 148.8 mV dec^{-1}), Cr_2Te_3 (-0.404 V, 96.1 mV dec^{-1}), and the mechanically mixed MnTe/Cr_2Te_3 catalyst (-0.459 V, 78.5 mV dec^{-1}). Additionally, the 5% Cr-doped MnTe sample showed an overpotential of -0.520 V at 10 mA cm^{-2} (Fig. S4), which was notably lower than that of pure MnTe. This improvement may

Published on 16 August 2025. Downloaded by Yunnan University on 8/23/2025 4:22:07 PM.

Nanoscale Accepted Manuscript

View Article Online
DOI: 10.1039/D5NR02857D

arise from early-stage structural modification or partial phase evolution. In contrast, the 10 at.% sample clearly forms a Cr_2Te_3/MnTe/Cr_2Te_3 heterojunction, which delivers the best performance. These results suggest that the enhanced activity is mainly associated with the combined effects of increased Cr content and heterojunction formation.

Fig. 4c showed the Nyquist plots of the samples measured at an applied potential of -0.4 V vs. RHE. The Cr_2Te_3/MnTe/Cr_2Te_3 heterojunction exhibited a smaller semicircular radius compared to the mechanically mixed MnTe/Cr_2Te_3 catalyst, suggesting lower interfacial resistance and faster interfacial charge transfer kinetics. This implies that the heterointerface promoted efficient charge transfer across the interface, reducing the overall interfacial resistance. These impedance results were consistent with the LSV data.

Long-term stability is a critical requirement for practical HER catalysts. During the I-t stability test conducted at a constant potential of -0.4 V vs. RHE for 4000 s (Fig. 4d), the Cr_2Te_3/MnTe/Cr_2Te_3 heterojunction demonstrated excellent HER stability. Furthermore, no significant morphological changes were observed in the catalyst before and after the electrolysis (Fig. S5), confirming its structural integrity and durability during prolonged operation. Additionally, as demonstrated in Table S1, the Cr_2Te_3/MnTe/Cr_2Te_3 heterostruction exhibits intermediate-to-high HER activity compared to previously reported electrocatalysts. The electrochemically active surface area (ECSA) of MnTe/Cr_2Te_3 heterojunction was evaluated using the double-layer capacitance (C_{dl}) method. As shown in Fig. S6, with the scan rate increasing from 20 to 100 mV s^{-1}, both the anodic and cathodic currents gradually increased, resulting in a series of nested CV curves. The linear fit of Δ j versus scan rate allowed us to extract C_{dl} (0.0347 mF cm^{-2}), which serves as an effective indicator of the relative ECSA, enabling normalization of the HER activity for intrinsic performance

Published on 16 August 2025. Downloaded by Yunnan University on 8/23/2025 4:22:07 PM.

Nanoscale Accepted Manuscript

View Article Online
DOI: 10.1039/D5NR02857D

comparison, in line with previous studies.[29-31]

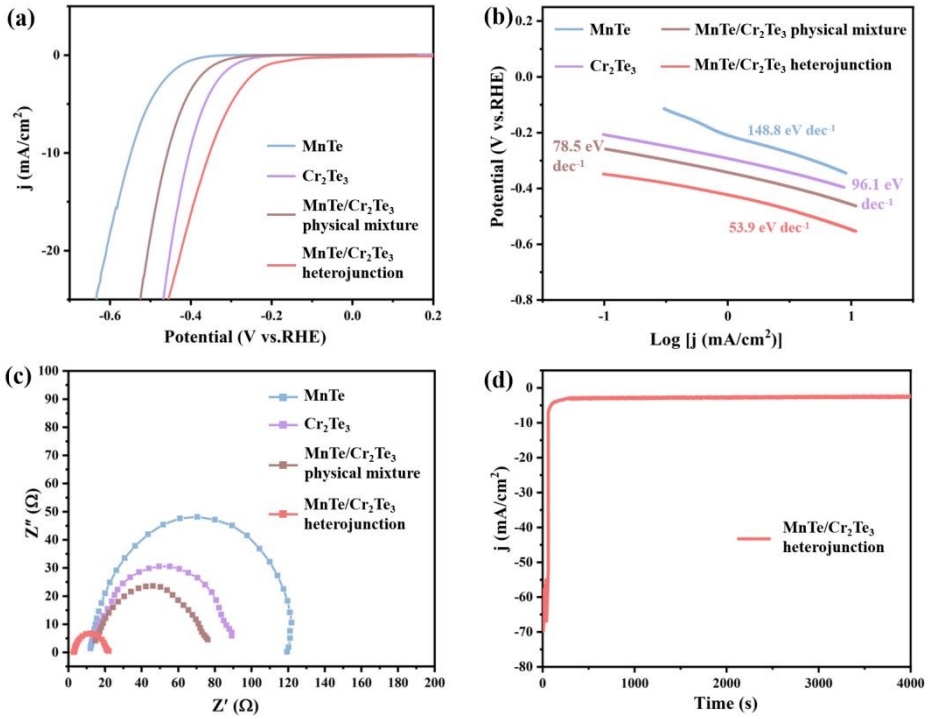

Fig. 4. (a) LSV curves of MnTe, Cr_2Te_3, MnTe/Cr_2Te_3 physical mixture, and MnTe/Cr_2Te_3 heterojunction. (b) Tafel plots for different catalysts vs. RHE. (c) Nyquist plots of samples measured at -0.4 V vs. RHE. (d) I-t curve of MnTe/Cr_2Te_3 heterojunction recorded over 4000 s.

3.3. Interfacial Mechanism and Electronic Modulation in HER Catalysis

To understand the origin of the enhanced HER activity observed in the Cr-doped MnTe/Cr_2Te_3 heterostructure, a series of DFT calculations were performed focusing on interfacial charge distribution, electronic structure modulation, and hydrogen adsorption behavior. As shown in Fig. 5a, the calculated charge density difference of the MnTe/Cr_2Te_3 interface clearly illustrates the direction of interfacial electron transfer. The yellow regions represent electron accumulation, while the blue regions correspond to electron depletion. The spatially asymmetric distribution of charge demonstrates that electrons are transferred from the metallic Cr_2Te_3 caps to the semiconducting

Published on 16 August 2025. Downloaded by Yunnan University on 8/23/2025 4:22:07 PM.

Nanoscale Accepted Manuscript

View Article Online
DOI: 10.1039/D5NR02857D

MnTe region, forming an internal electric field across the heterojunction. This interfacial potential gradient is expected to accelerate charge separation and promote HER kinetics.

To elucidate the structural stability and site preference of Cr dopants in MnTe, we constructed two representative doping models: (i) substitutional doping where a Cr atom replaces a Mn atom (Fig. 5b) and (ii) interstitial doping where Cr occupies an octahedral void in the MnTe lattice (Fig. 5c). The calculated formation energies indicate that substitutional doping (E = -106.8052 eV) is thermodynamically more favorable than interstitial incorporation (E = -102.4127 eV), suggesting that Cr^{3+} ions are more likely to substitute Mn^{2+} ions rather than occupy interstitial positions.

The impact of Cr doping on the electronic structure of MnTe was further investigated by projected density of states (PDOS) analysis. As shown in Fig. 5d, pristine MnTe exhibits a relatively sparse density of states near the Fermi level (E_f), particularly in the conduction band, which limits its intrinsic conductivity. Upon Cr substitution, new Cr 3*d* states emerge near E_f, and the Mn 2*p* and Te 3*d* contributions also become more delocalized, indicating enhanced carrier density and improved electrical conductivity. These modifications facilitate more efficient charge transport during HER.

Electronic structure analysis of the MnTe/Cr_2Te_3 heterojunction (Fig. 5e) further reveals strong orbital hybridization between the semiconducting MnTe and the metallic Cr_2Te_3. The Cr 3*d* states partially fill the bandgap of MnTe, resulting in a semiconductor-to-metal transition at the interface. This facilitates efficient interfacial charge transport and activation of additional catalytic sites. These findings are consistent with experimental observations of interfacial electron transfer confirmed by XPS and Bader charge analyses.

Published on 16 August 2025. Downloaded by Yunnan University on 8/23/2025 4:22:07 PM.

Nanoscale Accepted Manuscript

View Article Online
DOI: 10.1039/D5NR02857D

To directly evaluate the catalytic performance, we calculated the ΔG_{H^*} at Mn, Te, and Cr sites on MnTe, Cr_2Te_3, and the MnTe/Cr_2Te_3 heterostructure. As summarized in Table S2 and shown in Fig. 5f, pristine MnTe exhibits a strongly negative ΔG_{H^*} (-0.49 eV), indicating overly strong H* binding that may hinder desorption. Cr_2Te_3, by contrast, shows a weaker H* interaction with ΔG_{H^*} of +0.58 eV. Notably, the MnTe/Cr_2Te_3 interface yields a nearly thermoneutral ΔG_{H^*} of +0.04 eV, which is considered ideal for HER.[32] This confirms that the Mn site is the most favorable hydrogen adsorption site in the heterostructure, and highlights the role of interface engineering in optimizing reaction kinetics.

In brief, DFT calculations demonstrate that Cr-doped MnTe and the MnTe/Cr_2Te_3 heterostructure synergistically optimize hydrogen adsorption behavior and reaction pathway energy barriers through electronic structure modulation and the construction of electron redistribution interfaces, leading to enhanced HER reaction kinetics. These results offer valuable guidance for designing high-performance HER heterostructure catalysts.

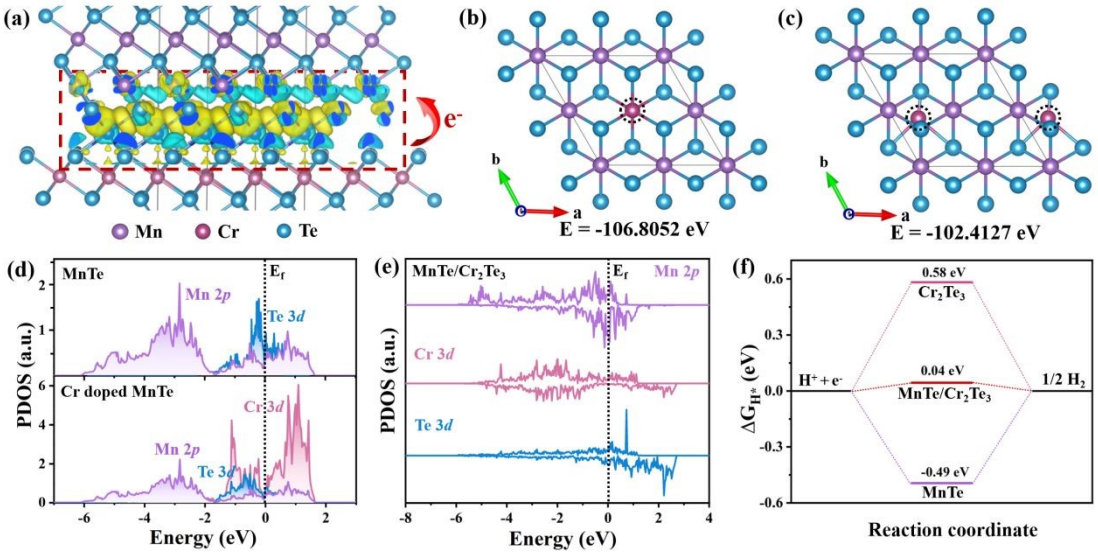

Published on 16 August 2025. Downloaded by Yunnan University on 8/23/2025 4:22:07 PM.

Nanoscale Accepted Manuscript

View Article Online
DOI: 10.1039/D5NR02857D

Fig. 5. (a) Calculated surface electrostatic potential distribution between MnTe and Cr_2Te_3. (Yellow: electron-rich areas; Blue: charge-depleted regions). (b,c) Top-view structural models of Cr-doped MnTe via (b) substitutional (Cr substituting Mn, purple atom) and (c) interstitial doping (Cr in octahedral void, pink atom), with corresponding doping formation energies. (d) Calculated PDOS for pristine MnTe and Cr-substituted MnTe. (e) Calculated PDOS of MnTe/Cr_2Te_3 heterojunction. (f) Calculated ΔG_{H*} on MnTe, Cr_2Te_3, MnTe/Cr_2Te_3 heterojunction.

4. Conclusion

In summary, we have successfully designed and synthesized Cr-doped MnTe and an epitaxial Cr_2Te_3/MnTe/Cr_2Te_3 metal-semiconductor-metal heterojunction via a solution-based method, achieving a highly efficient HER electrocatalyst. Structural characterizations confirmed the successful incorporation of Cr^{3+} cations into the MnTe lattice and the formation of high-quality interfaces. The Cr doping and heterostructure construction significantly modulate the electronic structure and facilitate interfacial charge redistribution. These modifications synergistically optimize the hydrogen adsorption free energy and reduce the kinetic barriers of key HER reaction steps. The resulting heterostructure catalyst demonstrates enhanced HER activity, with a low overpotential of -0.354 V at 10 mA cm^{-2} and a Tafel slope of 53.9 mV dec^{-1}. This work provides valuable guidance for the rational design and synthesis of high-performance HER electrocatalysts with tailored electronic structures and engineered interfaces.

Acknowledgments

This work was supported by the National Natural Science Foundation of China (52301244) and the Youth Science Foundation of Shanxi Province (202203021222218).

References

Published on 16 August 2025. Downloaded by Yunnan University on 8/23/2025 4:22:07 PM.

Nanoscale Accepted Manuscript

View Article Online
DOI: 10.1039/D5NR02857D

Published on 16 August 2025. Downloaded by Yunnan University on 8/23/2025 4:22:07 PM.

1 A. Liu, and S. Liu, *Renew. Sustain. Energy Rev.*, 2024, **202**, 114686.

2 Z. W. Seh, J. Kibsgaard, C. F. Dickens, I. B. Chorkendorff, J. K. Nørskov and T. F. Jaramillo, *Science*, 2017, **355**, eaad4998.

3 X. Zhao and K. Sasaki, *Acc. Chem. Res.*, 2022, **55**, 1226-1236.

4 H. Wu, C. Feng, L. Zhang, J. Zhang and D. P. Wilkinson, *Electrochem. Energy Rev.*, 2021, **4**, 473-507.

5 X. Wu, H. Zhang, J. Zhang and X. W. Lou, *Adv. Mater.*, 2021, **33**, 2008376.

6 L. Xiong, Y. Qiu, X. Peng, Z. Liu and P. K. Chu, *Nano Energy*, 2022, **104**, 107882.

7 Y. Zhang, Q. Zhou, J. Zhu, Q. Yan, S. X. Dou and W. Sun, *Adv. Funct. Mater.*, 2017, **27**, 1702317.

8 O. J. Amin, A. Dal Din, E. Golias, Y. Niu, A. Zakharov, S. C. Fromage, C. J. B. Fields, S. L. Heywood, R. B. Cousins, F. Maccherozzi, J. Krempaský, J. H. Dil, D. Kriegner, B. Kiraly, R. P. Campion, A. W. Rushforth, K. W. Edmonds, S. S. Dhesi, L. Šmejkal, T. Jungwirth and P. Wadley, *Nature*, 2024, **636**, 348-353.

9 A. Vijayana and N. Sandhyarani, *Energy Adv.*, 2024, **3**, 1092-1098.

10 Z. Wang, X. Chen, Y. Ding, X. Zhu, Z. Sun, H. Zhou, X. Li, W. Yang, J. Liu, R. He, J. Luo, T. Yu, M. Zeng and L. Fu, *J. Am. Chem. Soc.*, 2024, **147**, 1392-1398.

11 Y. Li, J. Li, W. Ai, J. Chen, T. Lu, X. Liao, W. Wang, R. Huang, Z. Chen, J. Wu, F. Cheng and H. Wang, *Angew. Chem. Int. Ed.*, 2024, **63**, e202407772.

12 S. Manzoor, S. Aman, M. M. Alanazi, S. A. M. Abdelmohsen, R. Y. Khosa, N. Ahmad, A. G. Abid, M. U. Nisa, R. Hua and A. H. Chughtai, *Appl. Nanosci.*, 2023, **13**, 5509-5519.

13 T. Tang, Z. Wang and J. Guan, *Chin. J. Catal.*, 2022, **43**, 636-678.

14 X. Gao, J. Qi, S. Wan, W. Zhang and Q. Wang, *Small*, 2018, **14**, 1803361.

15 A. Shan, X. Teng, Y. Zhang, P. Zhang, Y. Xu, C. Liu and H. Li, *Nano Energy*, 2022, **94**, 106913.

16 D. Khalafallah, F. Qiao, C. Liu, J. Wang, Y. Zhang, J. Wang, Q. Zhang and P. H. L. Notten, *Coord. Chem. Rev.*, 2023, **496**, 215405.

17 Z. M. Almarhoon, K. Jabbour, S. Manzoor, S. I. A. Shah, M. F. Ashiq, M. Y. U. Rehman, M. F. Ehsan, M. Najam-ul-Haq and M. N. Ashiq, *Fuel*, 2024, **363**, 130919.

Nanoscale Accepted Manuscript

View Article Online
DOI: 10.1039/D5NR02857D

18 T. Wang, B. Li, P. Wang, M. Xu, D. Wang, Y. Wang, W. Zhang, C. Qu and M. Feng, *J. Colloid Interface Sci.*, 2024, **672**, 715-723.

19 M. Cheng, H. Geng, Y. Yang, Y. Zhang and C. C. Li, Chem. *Eur. J.*, 2019, **25**, 8579-8584.

20 H. Li, L. Du, Y. Zhang, X. Liu, S. Li, C. C. Yang and Q. Jiang, *Appl. Catal. B Environ.*, 2024, **346**, 123749.

21 Y. Liu, J. Ding, F. Li, X. Su, Q. Zhang, G. Guan, F. Hu, J. Zhang, Q. Wang, Y. Jiang, B. Liu and H. B. Yang, *Adv. Mater.*, 2023, 35, 2207114.

22 G. Kresse and J. Furthmüller, Comput. *Mater. Sci.*, 1996, **6**, 15-50.

23 G. Kresse and J. Furthmüller, *Phys. Rev. B*, 1996, **54**, 11169-11186.

24 J. P. Perdew, K. Burke and M. Ernzerhof, Phys. *Rev. Lett.*, 1996, **77**, 3865-3868.

25 G. Kresse and D. Joubert, *Phys. Rev. B*, 1999, **59**, 1758-1775.

26 Q. Zhang, T. Xia, H. Huang, J. Liu, M. Zhu, H. Yu, W. Xu, Y. Huo, C. He, S. Shen, C. Lu, R. Wang, and S. Wang, *Nano Res. Energy*, 2023, **2**, e9120041.

27 C. Battistoni, G. Mattogno, E. Paparazzo and G. M. Ingo, *Surf. Coat. Technol.*, 2004, **29**, 105.

28 R. J. Iwanowski, M. H. Heinonen and B. Witkowska, *J. Alloys Compd.*, 2010, **491**, 13-17.

29 S. Zhao, S. S. Shen, L. Han, B. C. Tian, N. Li, W. Chen, and X. B. Li, *Rare Met.* 2024, **43**, 4038-4055.

30 X. Li, Q. Liu, F. Deng, J. Huang, L. Han, C. He, Z. Chen, Y. Luo, and Y. Zhu, *Appl. Catal. B: Environ.*, 2022, **314**, 121502.

31 S. Shen, X. Li, Y. Zhou, L. Han, Y. Xie, F. Deng, J. Huang, Z. Chen, Z. Feng, J. Xu, and F. Dong, *J. Mater. Sci. Technol.*, 2023, **155**, 148-159.

32 K. S. Exner, I. Sohrabnejad-Eskan and H. Over, *ACS Catal.*, 2018, **8**, 1864-1879.

Published on 16 August 2025. Downloaded by Yunnan University on 8/23/2025 4:22:07 PM.

Nanoscale Accepted Manuscript

View Article Online
DOI: 10.1039/D5NR02857D

Data Availability Statement

The authors confirm that the data supporting the findings of this study are available within the article and its supplementary materials

Published on 16 August 2025. Downloaded by Yunnan University on 8/23/2025 4:22:07 PM.

Nanoscale Accepted Manuscript